



H- and Dissociation in Ultra-hot Jupiters: A Retrieval Case Study of WASP-18b

Siddharth Gandhi^{1,2} , Nikku Madhusudhan¹ , and Avi Mandell³ 

¹Institute of Astronomy, University of Cambridge, Madingley Road, Cambridge, CB3 0HA, UK; Siddharth.Gandhi@warwick.ac.uk

²Department of Physics, University of Warwick, Coventry CV4 7AL, UK

³NASA Goddard Space Flight Center, Greenbelt, MA, USA

Received 2019 July 19; revised 2020 March 27; accepted 2020 March 27; published 2020 April 23

Abstract

Atmospheres of a number of ultra-hot Jupiters (UHJs) with temperatures $\gtrsim 2000$ K have been observed recently. Many of these planets show largely featureless thermal spectra in the near-infrared observed with the HST WFC3 spectrograph (1.1–1.7 μm) even though this spectral range contains strong H₂O opacity. Recent works have proposed the possibility of H- opacity masking the H₂O feature and/or thermal dissociation of H₂O causing its apparent depletion at the high temperatures of UHJs. In this work, we test these hypotheses using observations of the exoplanet WASP-18b as a case study. We report detailed atmospheric retrievals of the planet using the HyDRA retrieval code, extended to include the effects of H- opacity and thermal dissociation. We report constraints on the H₂O, CO, and H- abundances as well as the pressure–temperature profile of the dayside atmosphere for retrievals with and without H-/dissociation for each data set. We find that the H₂O and H- abundances are relatively unconstrained given the featureless WFC3 spectra. We do not conclusively detect H- in the planet, contrary to previous studies that used equilibrium models to infer its presence. The constraint on the CO abundance depends on the combination of WFC3 and Spitzer data, ranging from solar to super-solar CO values. We additionally see signs of a thermal inversion from two of the data sets. Our study demonstrates the potential of atmospheric retrievals of UHJs, including the effects of H- and thermal dissociation of molecules.

Unified Astronomy Thesaurus concepts: [Exoplanet atmospheres \(487\)](#); [Spectroscopy \(1558\)](#); [Radiative transfer \(1335\)](#); [Hot Jupiters \(753\)](#); [Exoplanets \(498\)](#)

1. Introduction

Recent observations of hot Jupiters are providing some of the most precise atmospheric spectra of exoplanets to date. Such data have provided important constraints on the atmospheric parameters, e.g., composition and temperature profile, thanks to instruments such as the HST WFC3 spectrograph (Deming et al. 2013; Madhusudhan 2019). A new class of irradiated giant planets, that of ultra-hot Jupiters (UHJs), has emerged recently. These planets have dayside temperatures exceeding ~ 2000 K owing to strong incident stellar flux due to their short orbital periods. Observations of such objects have revealed that many of these atmospheres show no significant features in the WFC3 bandpass (e.g., Sheppard et al. 2017; Arcangeli et al. 2018, 2019; Kreidberg et al. 2018; Lothringer et al. 2018; Mansfield et al. 2018). With such featureless spectra, constraints on species such as H₂O have been minimal, and only upper limits have generally been derived.

Several hypotheses have been put forward to explain the lack of strong H₂O features and generally featureless spectra for UHJs. A high C/O ratio has been invoked as a possible explanation for muted H₂O features in many hot Jupiters, both in transmission and emission (e.g., Madhusudhan et al. 2011, 2014; Sheppard et al. 2017; Pinhas et al. 2019). Previous studies have shown that a super-solar atmospheric C/O ratio can deplete H₂O in the atmosphere for temperatures $\gtrsim 1200$ K (e.g., Madhusudhan 2012; Moses et al. 2013; Drummond et al. 2019). In this case, the oxygen preferentially binds to form CO when C/O $\gtrsim 1$, thus significantly reducing the overall H₂O abundance. The low H₂O abundance, in turn, can lead to weaker features in the HST WFC3 band (1.1–1.7 μm) where H₂O has strong opacity.

An alternate explanation is the thermal dissociation of H₂O in UHJs. Equilibrium models of UHJs have revealed that the dissociation of species such as H₂O and the formation of H- may

play an important role in determining the emergent spectrum (Arcangeli et al. 2018; Lothringer et al. 2018; Parmentier et al. 2018). The H- is formed in irradiated environments rich in hydrogen and free electrons, and it is in fact the dominant source of opacity in stars cooler than 7000 K (Wishart 1979; Bell & Berrington 1987). The H- ion possesses broad continuum opacity in the 1.1–1.7 μm WFC3 band. This opacity can fill in the gap in between the H₂O feature at ~ 1.4 μm and result in featureless spectra (Parmentier et al. 2018). In addition, at high temperatures, thermal dissociation of H₂O would act to diminish the H₂O abundance and further mute H₂O features below expected levels (Arcangeli et al. 2018). Very high temperatures are required for both H- opacity and thermal dissociation to be significant, but UHJs such as WASP-121b, WASP-18b, WASP-12b, Kepler-13Ab, HAT-P-7b, and KELT-9b have equilibrium temperatures in excess of ~ 2000 K and, therefore, warrant consideration of these contributions (e.g., Arcangeli et al. 2018; Kitzmann et al. 2018; Kreidberg et al. 2018; Lothringer et al. 2018; Mansfield et al. 2018). Thermal dissociation is generally also favored by lower pressures (e.g., Parmentier et al. 2018). However, it is unclear whether the absence of an H₂O feature in the WFC3 bandpass for UHJs can be solely attributed to these two factors—some UHJs with similar dayside temperatures (e.g., KELT-1b, Kepler-13Ab) do in fact show strong H₂O absorption (Beatty et al. 2017b, 2017a; Parmentier et al. 2018).

In this work, we assume an agnostic position a priori on which effect is dominant in UHJs. We investigate evidence for the above hypotheses by performing spectral retrievals of a well-known UHJ, WASP-18b (Sheppard et al. 2017; Arcangeli et al. 2018). Previous retrievals of WASP-18b have proposed a high C/O ratio as an explanation for the observed spectrum, which does not show strong H₂O features in the WFC3 band (Sheppard et al. 2017). However, their derived CO abundance

implied a very high metallicity of 283_{-138}^{+395} solar. On the other hand, Arcangeli et al. (2018) explored a grid of equilibrium models to propose H- and dissociation as a potential explanation for the featureless spectrum. General circulation models have also been used to explain the phase curve of WASP-18b (Arcangeli et al. 2019). We assess evidence for the two proposed hypotheses by conducting retrievals on the three HST WFC3 data sets available for this planet (Sheppard et al. 2017; Arcangeli et al. 2018, 2019) along with the associated Spitzer photometry between 3.6 and 8 μm (Nymeyer et al. 2011; Maxted et al. 2013; Sheppard et al. 2017).

We explore different proposed scenarios to explain the emission spectrum of WASP-18b. We retrieve the abundances of species such as H₂O and CO as free parameters rather than enforcing chemical equilibrium, which other studies have done. Our parametric temperature profile explores isothermal as well as inverted and non-inverted profiles to determine the best fit to the observations. We additionally include thermal dissociation and H- opacity in our model to explore their effects on the retrieved parameters both separately and in tandem over multiple separate retrievals. We perform extensive retrievals for three HST WFC3 data sets for the dayside emission spectrum of WASP-18b, namely from Sheppard et al. (2017), Arcangeli et al. (2018), and Arcangeli et al. (2019). All of these data sets represent a measurement of the dayside flux from WASP-18b, but Arcangeli et al. (2019) produce their spectral data set by binning the phase-resolved spectra between phases of 0.4-0.45 and 0.55-0.6, just before and after secondary eclipse, rather than determining the best estimate of the spectrum during eclipse itself, as is standard in secondary eclipse analyses. Therefore, the Arcangeli et al. (2019) data set is probing a slightly different portion of the dayside disk of the planet compared with the other two data sets. The bulk planetary conditions may be roughly similar between the data sets, though an exact comparison of the retrieved properties from the Arcangeli et al. (2019) data set and the other two data sets is not our goal.

In what follows, we describe the modeling and retrieval method in Section 2. This is followed by the results for the retrievals conducted with and without H- and dissociation in Section 3. We discuss the retrieved parameters and compare and contrast each retrieval. Finally, we discuss the conclusions and future directions in Section 4.

2. Methods

Here, we describe the methods used for the retrieval of the emission spectra of UHJs. We build upon the HyDRA retrieval code (Gandhi & Madhusudhan 2018) and generalize it to UHJs. In particular, the HyDRA framework is extended to model the atmospheres of UHJs by the inclusion of thermal dissociation and H- opacity. Previous studies have shown the importance of these at temperatures in excess of ~ 2000 K (Arcangeli et al. 2018; Lothringer et al. 2018; Parmentier et al. 2018). The additions to the retrieval model are discussed below in Sections 2.1 and 2.2.

The composition and pressure–temperature (P–T) profile are free parameters in the model. For the chemical composition, we do not make any assumptions of chemical equilibrium; instead, we derive the abundances with uniform priors with no a priori constraints. The P–T profile has been parameterized using the method outlined in Madhusudhan & Seager 2009. The six free parameters that parameterize the P–T profile freely allow for

inversions in the atmosphere. Through these parameters, we are able to explore a wide range of inverted, non-inverted, and isothermal profiles to best fit the observations. We also assume a plane–parallel geometry with the assumption that the atmosphere is in hydrostatic equilibrium and local thermodynamic equilibrium. The emergent flux out of the atmosphere is calculated from double-ray integration of emergent rays of radiation out of the atmosphere as discussed in Gandhi & Madhusudhan (2018). To generate the stellar spectrum, we use the Kurucz model grid (Kurucz 1979). The Bayesian parameter estimation is performed using the Nested Sampling algorithm implemented in the MultiNest package (Feroz & Hobson 2008; Feroz et al. 2009; Buchner et al. 2014). Further details on the retrieval and the model setup can be found in Gandhi & Madhusudhan (2018).

The chemical opacities have been derived using high-temperature line lists for the various species. These species include H₂O, CO, CO₂, TiO, and VO, which are expected to be prominent in ultra-hot H₂ dominated atmospheres (Madhusudhan 2012). The line lists for H₂O, CO, and CO₂ have been obtained from the HITEMP database (Rothman et al. 2010). The high-temperature line lists for TiO and VO have been obtained from the ExoMol database (McKemmish et al. 2016, 2019; Tennyson et al. 2016). The opacity due to the presence of H- has been calculated following John (1988) and Wishart (1979; see Section 2.2). Each molecular line has been spectrally broadened by temperature and pressure resulting in a Voigt profile as a function of wavelength (Gandhi & Madhusudhan 2017). The molecular cross sections for each of the prominent species has been precomputed at a wavenumber spacing of 0.1 cm^{-1} between 0.4 and 50 μm with temperatures and pressures ranging from 300 to 3500 K and 10^2 – 10^{-5} bar, respectively. We additionally include opacity from collisionally induced absorption from H₂ to H₂ and H₂–He interactions (Richard et al. 2012).

2.1. Thermal Dissociation

Ultra-hot giant planets have temperatures in excess of 2000 K, where many molecular species may begin to thermally dissociate (Arcangeli et al. 2018; Lothringer et al. 2018; Parmentier et al. 2018). Arcangeli et al. (2018) in particular have argued that temperatures in excess of ~ 2000 – 2500 K can result in the thermal dissociation of molecular species. This may result in significant depletion of species such as H₂O in the upper atmosphere, which acts to lower the infrared photosphere deeper into the atmosphere. In addition, the depletion in the upper atmosphere can also reduce the extent of the $\tau_{\nu} \sim 1$ surface (Parmentier et al. 2018). This can thus reduce the extent of spectral features and, therefore, significantly alter the emission spectra for such ultra-hot planets. This has been used to explain many of the featureless WFC3 spectra for some of the hottest systems such as WASP-121b, WASP-18b, and WASP-103b (Arcangeli et al. 2018; Kreidberg et al. 2018; Parmentier et al. 2018). We therefore include thermal dissociation for H₂O, TiO, VO, and H-, which are expected to be susceptible to dissociation at such high temperatures.

We calculate the volume mixing fractions of these species as a function of pressure and temperature from the dissociation model developed by Parmentier et al. (2018). The volume mixing fraction $A_i(P, T)$ of species i is given by

$$\frac{1}{A_i^{0.5}} = \frac{1}{A_{0,i}^{0.5}} + \frac{1}{A_{d,i}^{0.5}}. \quad (1)$$

$A_{0,i}$ is the deep atmosphere (undissociated) abundance and

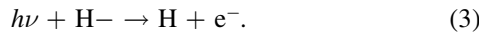
$$\log(A_{d,i}) = \alpha_i \log(P) + \beta_i/T - \gamma_i, \quad (2)$$

for pressure P (bar) and temperature T (K) and parameters α_i , β_i and γ_i , which are fits to the equilibrium abundances at solar composition (Parmentier et al. 2018). Using the deep atmosphere abundance $A_{0,i}$ for each species i , we calculate the dissociated volume mixing ratio $A_i(P, T)$ according to the pressure and temperature through Equations (1) and (2). This is done for each layer of the model atmosphere resulting in a volume mixing fraction that is a function of atmospheric depth. Thermal dissociation of CO has not been included here as it does not readily dissociate at the temperatures seen on WASP-18b and other ultra-hot Jupiters (e.g., Lodders & Fegley 2002; Arcangeli et al. 2018; Parmentier et al. 2018). In our retrieval, the undissociated abundance priors for H₂O, TiO, VO, and H-span $\log(A_{0,i}) = -15$ and 0. Our upper bound for the H- prior is restricted to $\log(\text{H-}) = -7$ in our fiducial retrieval given that equilibrium models assuming solar composition predict a lower abundance of $\log(\text{H-}) \approx -8.3$ (e.g., Parmentier et al. 2018). This parametric model for thermal dissociation is most accurate near solar composition, but we should highlight the fact that our retrieval explores a wider range of composition. The dissociated H- abundance in particular may be inaccurate away from solar abundance chemistry as it depends strongly on the free electron abundance (Arcangeli et al. 2018; Parmentier et al. 2018). In addition, we have also run retrievals including the effect of H₂ dissociation to study its effect on the retrieved parameters.

2.2. H- Opacity

At the high temperatures of UHJs, H- may be present in the atmosphere and, thus, affect the emergent spectrum due to its strong cross section in the near-infrared (Arcangeli et al. 2018; Lothringer et al. 2018; Parmentier et al. 2018). The H- cross section arises as a result of two separate sources of opacity: bound-free photodetachment and free-free transitions. Both of these sources of opacity result in broad features in the cross section, unlike with molecular cross sections, which consist of many millions of broadened transition lines. The bound-free transitions have strong absorption at $\lambda < 1.64 \mu\text{m}$, the photodetachment threshold wavelength, and are in fact the dominant source of opacity in cool stars (Wishart 1979). At longer wavelengths, the free-free transitions are the only contributors to the cross section of H-. Both of these opacity contributions are summed to give the total cross section of H-. Figure 1 shows the abundance weighted cross section at a representative temperature of 2900 K and pressure of 0.33 bar. The abundances are calculated from the dissociation model in Section 2.1 assuming a solar composition atmosphere.

The bound-free opacity arises due to the absorption of a photon by H-



The cross section of this reaction, $\sigma_{\text{H-}}$, is given by

$$\sigma_{\text{H-}}(\lambda < \lambda_0) = 10^{-18} \lambda^3 \left(\frac{1}{\lambda} - \frac{1}{\lambda_0} \right)^{3/2} f(\lambda) \text{cm}^2, \quad (4)$$

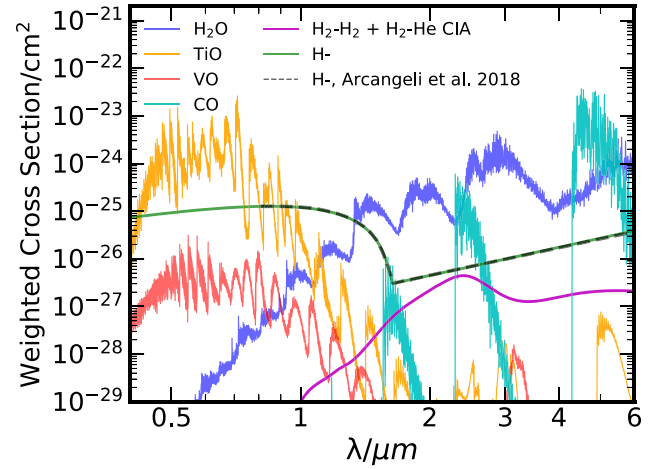
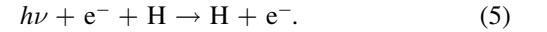


Figure 1. Abundance weighted cross sections for the prominent species in our retrieval at a temperature of 2900K and pressure of 0.33 bar. The abundances have been calculated from the dissociation model by Parmentier et al. (2018) and the cross sections derived in Gandhi & Madhusudhan (2017). The H-opacity is calculated in Section 2.2. We also show the abundance weighted H-cross section from Arcangeli et al. (2018).

where λ represents the wavelength in μm , $\lambda_0 = 1.6419 \mu\text{m}$ is the photodetachment threshold, and $f(\lambda)$ is a slowly varying function (John 1988). These bound-free transitions result in a cutoff in the opacity at the photodetachment threshold, with a strong cross section at $\lambda < \lambda_0$. This cutoff is of particular importance given that λ_0 is within the HST WFC3 bandpass (1.1–1.7 μm).

The free-free transitions on the other hand occur due to the following chemical interaction (Bell & Berrington 1987):



These transitions are important sources of infrared opacity for late spectral-type stars (Bell & Berrington 1987). This opacity may also be important in UHJs, particularly for the Spitzer photometric observations at $\lambda > 3 \mu\text{m}$ given that this cross section increases with wavelength. A more detailed study of the free-free absorption due to H- can be found in John (1988) and Bell & Berrington (1987). In our model, the combined opacity for both bound-free and free-free transitions is included, and we leave the volume mixing ratio of H- as a free parameter in the retrieval, which is used to compute the total opacity due to H-, including the effect of thermal dissociation as described earlier.

2.3. Retrieval Setup

We analyze both HST WFC3 and Spitzer observations (across the four channels) for WASP-18b using all three available dayside observations (Sheppard et al. 2017; Arcangeli et al. 2018, 2019). These HST and Spitzer observations are some of the most precise measurements of ultra-hot Jupiter emission available today. We note, as discussed in Section 1, that the Arcangeli et al. (2019) data set is derived from a slightly different part of the dayside disk of the planet, and hence, the retrieved properties from this spectrum may not be directly comparable to those from the other two data sets. Our retrievals for the Sheppard et al. (2017) data set do not include the final three data points in the WFC3 range, as Arcangeli et al. (2018) and Arcangeli et al. (2019) do not include data

Table 1
The Values for the WASP-18 System Used in This Work

WASP-18 System Parameter	Assumed Value in Retrieval
Planetary Radius/ R_J	1.19
Planetary Mass/ M_J	10.4
Stellar Effective Temperature/K	6430.0
Stellar Radius/ R_\odot	1.26
Stellar Mass/ M_\odot	1.46
Stellar Metallicity [Fe/H]	0.10

Note. We assume that the radius of Jupiter is 7.15×10^7 m.

beyond $1.6 \mu\text{m}$. This allows us to consistently retrieve each data set over the same range of observations. The Arcangeli et al. (2019) data set has been reconstructed adopting conservative error bars based on the Arcangeli et al. (2018) data. The 3.6 and $4.5 \mu\text{m}$ Spitzer data for the Arcangeli et al. (2018) and Arcangeli et al. (2019) data sets are obtained from Maxted et al. (2013), but Sheppard et al. (2017) reanalyzed these photometric data for their work and achieved significantly smaller uncertainties. For all three studies, the eclipse depths in the $5.8 \mu\text{m}$ and $8 \mu\text{m}$ channels were obtained from previous analyses by Nymeyer et al. (2011).

For each retrieval, we use 4000 evenly spaced wavelength points between 1.1 and $10.4 \mu\text{m}$ for our line-by-line calculations, encompassing both the WFC3 and Spitzer IRAC observations. The assumed planetary and stellar parameters are given in Table 1 and obtained from Shporer et al. (2019). To generate the stellar spectrum, we use the Kurucz model grid (Kurucz 1979; Castelli & Kurucz 2003). Each retrieval contains six free parameters for the P–T profile and five for the volume mixing fraction of H_2O , CO , CO_2 , TiO , and VO . The priors for these parameters are given in Table 2. An additional free parameter for the H- abundance is also included in some of the retrievals. H- is expected to be present at $\log(\text{H-}) \approx -8.3$ in the dayside atmospheres of UHJs (e.g., Arcangeli et al. 2018; Parmentier et al. 2018). Our fiducial case assumes an undissociated H- prior range $\log(\text{H-}) = -15$ to -7 , but we have also run retrievals with a wide H- prior extending this to $\log(\text{H-}) = 0$. The retrieval without H- or dissociation is similar to previous work (Sheppard et al. 2017), but we do not include CH_4 or HCN given that no evidence was seen for either of these species. In order to accurately retrieve the parameters and provide Bayesian evidences, we use the Nested Sampling algorithm MultiNest (Feroz & Hobson 2008; Feroz et al. 2009; Buchner et al. 2014). Further details on the forward model calculations and retrieval framework can be found at the beginning of Section 2 and in Gandhi & Madhusudhan 2018.

3. Results

Here, we discuss the results from retrievals of the emission spectrum of WASP-18b as considered by Sheppard et al. (2017), Arcangeli et al. (2018), and Arcangeli et al. (2019). We retrieved the WFC3 and Spitzer data with and without H- and dissociation included in the retrieval model to see the effect of each separately and together for each of the available data sets. For each data set, we perform five retrievals in the various combinations (see Table 3). Our fiducial model includes dissociation and H- with the undissociated prior for H- restricted to be from $\log(\text{H-}) = -15$ to -7 . The posterior distributions for these retrievals are given in Section 3. Our

Table 2
The Priors for the Parameters in the Retrievals of WASP-18b Carried Out in This Work

Parameter	Prior Range
$\log(\text{H}_2\text{O})$, $\log(\text{CO})$, $\log(\text{CO}_2)$, $\log(\text{TiO})$, $\log(\text{VO})$	-15 – 0
$\log(\text{H-})$	-15 – 7^a
$T_{100 \text{ mb/K}}$	300 – 4000
$\alpha_1/\text{K}^{-1/2}$	0 – 1
$\alpha_2/\text{K}^{-1/2}$	0 – 1
$\log(P_1/\text{bar})$	-6 – 2
$\log(P_2/\text{bar})$	-6 – 2
$\log(P_3/\text{bar})$	-2 – 2

Notes. Each of these priors are uniform in the range given.

^a We also run retrievals extending the undissociated H- prior to $\log(\text{H-}) = 0$.

unrestricted wide prior retrieval with H- and thermal dissociation considers an undissociated H- prior of $\log(\text{H-}) = -15$ to 0 . Table 3 summarizes the constraints on the various atmospheric parameters from these retrievals, showing the $P = 100$ mb temperature, H_2O , CO , and H- abundances for each data set. The spectral fit for the fiducial retrieval is shown for each data set in Figure 2.

Figure 2 shows a well-fit planet/star flux ratio for both the WFC3 and Spitzer observations (inset in the figure). The top left panel shows the data sets, along with blackbody curves for WASP-18b for various temperatures. The HST WFC3 points for all three show a relatively featureless spectrum, and thus, the constraints on the spectroscopically active species in this spectral range are minimal as shown in Figure 3. The H-abundance shows a bimodal distribution for the Sheppard et al. (2017) data set. This is because the dip in the spectrum at the red end of the WFC3 observations, as shown in Figure 4, can be explained by strong absorption due to either CO or H-. The Spitzer data for the Sheppard et al. (2017) and Arcangeli et al. (2018) data sets additionally constrain CO due to its feature in the $4.5 \mu\text{m}$ band. The CO_2 , TiO , and VO abundances do not show any significant constraints from the current observations given their likely trace abundances and weak features at the wavelengths probed.

The P–T profiles for each of the retrievals also agree well with each other, with the most well-constrained temperature for each of the data sets in the photosphere at $P \sim 100$ mbar as shown in Figure 5. This is as we would expect given the similarity of the data. For each data set, we find $T_{100\text{mb}}$ between ~ 2800 – 3000 K as expected from the blackbody curves in the top left panel of Figure 2. These also agree remarkably well with the expected equilibrium temperature of WASP-18b without significant redistribution ($T \approx 2850$ K). We see a slight thermal inversion with the Sheppard et al. (2017) and Arcangeli et al. (2019) data sets, but we see a more isothermal profile with the Arcangeli et al. (2018) data. However, the Arcangeli et al. data sets do allow for inverted and non-inverted temperature profiles due to uncertainties in the retrieved P–T profile. We will now discuss some key differences between the retrievals along with the implications below.

3.1. H_2O Abundances

We only retrieve weak constraints and upper limits for the H_2O abundance, even with the inclusion of H- and dissociation. This is due to the relatively featureless spectrum seen in all

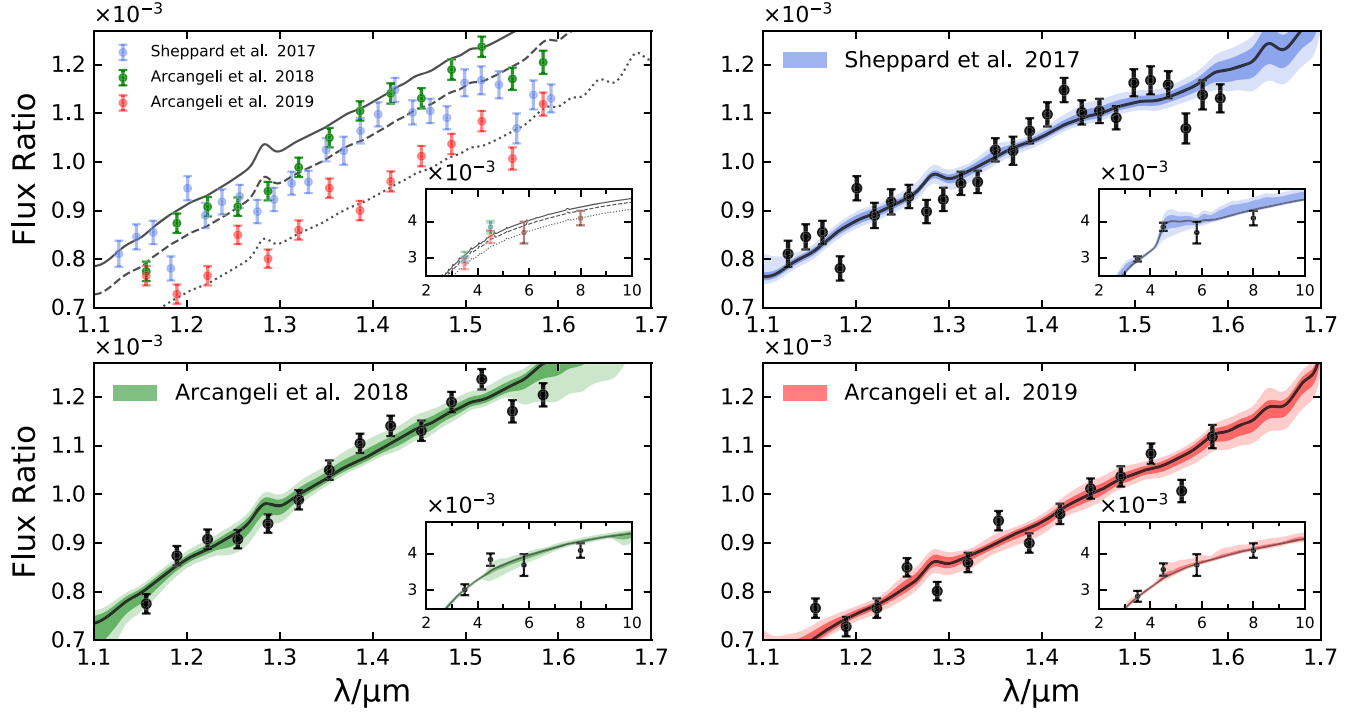


Figure 2. Thermal emission spectra (planet/star flux ratios) of WASP-18b from the different data sets and model fits from retrievals. The main panel shows the HST WFC3 data (1.1–1.7 μm), and the inset in each panel shows the Spitzer IRAC photometric points. The top left panel shows the three data sets together with blackbody curves at 2800 K (dotted line), 2900 K (dashed line), and 2950 K (solid line). The other three panels show the observed spectra from each data set and the corresponding model fits from retrievals with H- and dissociation. The dark and light colors indicate the 1σ and 2σ uncertainty, respectively, and the solid line shows the median best-fit curve for each. The final three HST WFC3 points for the Sheppard et al. (2017) data set have not been included into our retrievals for comparisons given that the other two data sets do not have data at these wavelengths.

Table 3
Retrieved Temperature and Abundance Parameters for the Various Retrievals Conducted on the Emission Spectrum of WASP-18b

Data Set	Retrieval	$T_{100\text{ mb}}/\text{K}$	$\log(\text{H}_2\text{O})$	$\log(\text{CO})$	$\log(\text{H}^-)$	Model Comparison
Sheppard et al. (2017)	No H-, No dissociation	2829^{+36}_{-48}	< -5.9	$-0.58^{+0.24}_{-0.35}$	–	Reference value
	Dissociation, no H-	2805^{+32}_{-44}	< -6.1	$-0.41^{+0.14}_{-0.25}$	–	Disfavored by 2.0σ
	H-, No dissociation	2804^{+47}_{-99}	< -0.70	$-1.10^{+0.60}_{-6.8}$	< -3.9	Disfavored by 2.6σ
	H-, dissociation (wide prior)	3005^{+31}_{-23}	$-7.3^{+2.8}_{-4.0}$	$-2.70^{+0.45}_{-0.57}$	$-3.4^{+2.1}_{-2.2}$	Disfavored by 3.1σ
	H-, dissociation (fiducial)	2810^{+33}_{-37}	< -5.7	$-0.41^{+0.15}_{-0.28}$	< -7.6	Disfavored by 2.4σ
Arcangeli et al. (2018)	No H-, No dissociation	2849^{+64}_{-46}	< -0.7	$-1.2^{+1.0}_{-7.0}$	–	Reference value
	Dissociation, no H-	2858^{+59}_{-55}	< -0.5	$-2.5^{+2.2}_{-6.8}$	–	Disfavored by 1.6σ
	H-, No dissociation	2868^{+53}_{-54}	< -0.6	$-2.0^{+1.8}_{-6.4}$	< -3.1	Disfavored by 1.6σ
	H-, dissociation (wide prior)	2907^{+13}_{-67}	< -0.4	$-5.4^{+4.7}_{-4.7}$	< -1.5	Disfavored by 1.9σ
	H-, dissociation (fiducial)	2889^{+30}_{-78}	< -0.5	$-4.0^{+3.6}_{-3.6}$	< -7.5	Disfavored by 1.5σ
Arcangeli et al. (2019)	No H-, No dissociation	2803^{+18}_{-31}	$-5.6^{+3.3}_{-4.4}$	< -0.3	–	Reference value
	Dissociation, no H-	2819^{+12}_{-11}	$-6.5^{+3.1}_{-4.0}$	< -0.3	–	Disfavored by 1.3σ
	H-, No dissociation	2800^{+20}_{-33}	$-4.9^{+3.0}_{-4.5}$	< -0.3	< -2.5	Favored by 1.1σ
	H-, dissociation (wide prior)	2819^{+12}_{-10}	$-6.5^{+3.0}_{-4.1}$	< -0.3	< -1.4	Disfavored by 1.3σ
	H-, dissociation (fiducial)	2819^{+12}_{-10}	$-6.5^{+3.1}_{-4.1}$	< -0.3	< -7.3	Disfavored by 1.3σ

Note. In each case where there was a peak in the posterior distribution, the retrieved median value is shown with its 1σ uncertainty and where there was no observable peak, the 2σ upper limit is shown. We report median values for the abundances as conservative estimates, even though the modal values are significantly higher than the median values in some cases. In models with thermal dissociation, the 100 mbar abundance is shown. The H- prior in the fiducial case was restricted to be between $\log(\text{H}^-) = -15$ and -7 , whereas in the wide prior and H- without dissociation case, the H- range was between $\log(\text{H}^-) = -15$ and -0 . We also show the Bayesian comparison for each model versus our reference case.

three data sets. Figure 2 shows the fit to the 1.1–1.7 μm WFC3 data. At these wavelengths, the opacity from H_2O , along with perhaps H-, is expected to be dominant over any other. Figure 3 shows the retrieved H_2O abundance (undissociated) at a

reference pressure of $P = 100$ mbar. All of the retrievals that were run across all of the data sets do not show strong constraints on H_2O due to the featureless blackbody-like WFC3 spectra (see Table 3). Despite some tentative peaks in the

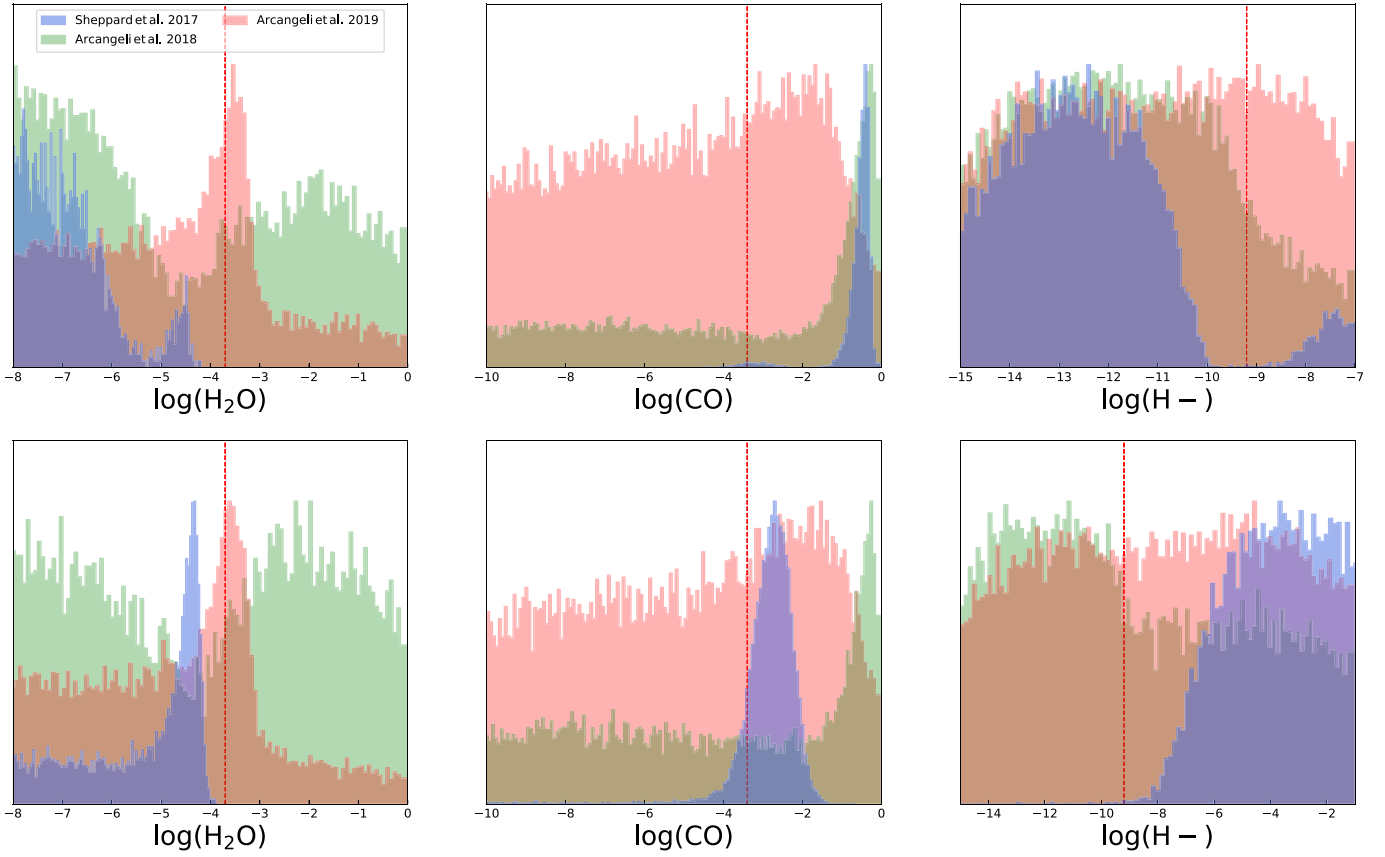


Figure 3. Posterior probability distributions of undissociated H_2O , CO , and H^- abundances for the various retrievals conducted. The top panels show the fiducial case where the H^- prior was restricted to be between $\log(\text{H}^-) = -15$ and -7 , whereas the bottom panel shows the wide prior case where the upper H^- prior was extended to $\log(\text{H}^-) = -0$. In each retrieval shown, the H_2O and H^- were thermally dissociated with pressure and temperature according to the model in Section 2.1. The red dashed line shows the expected abundance for each of the species assuming chemical equilibrium with solar elemental abundances (Parmentier et al. 2018).

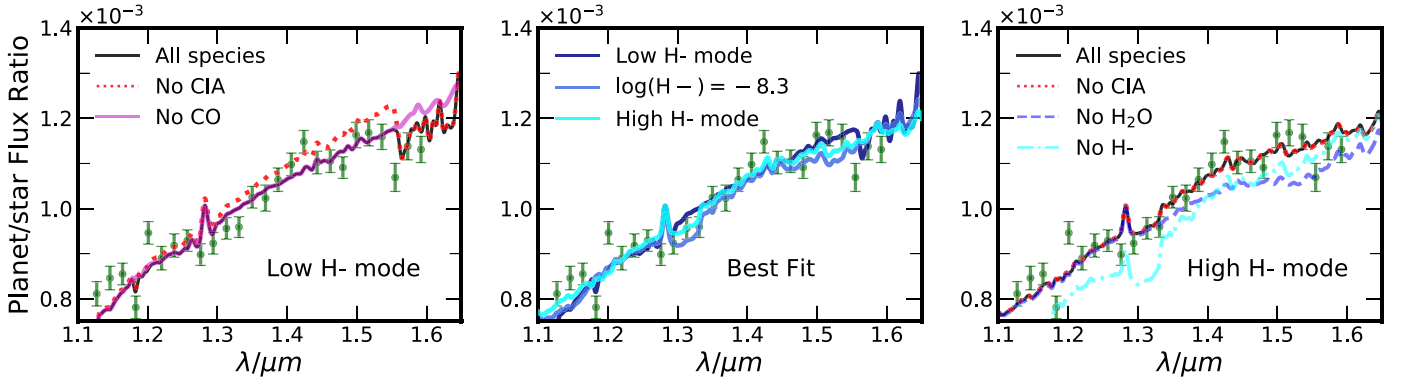


Figure 4. Best-fit models for the retrievals of the Sheppard et al. (2017) data set with the different opacity sources removed. The left panel shows the low H^- abundance mode, and the right panel shows the high H^- mode. The middle panel shows the best-fit cases for both alongside a best-fit model with the H^- abundance fixed to the solar equilibrium value (Parmentier et al. 2018).

posterior distributions, H_2O cannot be conclusively detected in our retrievals. The inclusion of H^- or dissociation into our model does not alter the H_2O abundances and all still have wide uncertainties on the abundance. In fact, as a general trend across all of the data sets, the inclusion of H^- and dissociation increases the uncertainty on the retrieved abundances slightly due to the extra parameter.

The Sheppard et al. (2017) data show upper limits on the H_2O at sub-solar abundance, but there is no definitive detection of H_2O . This is in agreement with retrievals published in their

original study. Our new retrievals with H^- and dissociation also only show a sub-solar upper limit on the H_2O . The fiducial case in Figure 3 does show a peak at $\log(\text{H}_2\text{O}) \sim -4.5$, but with a long tail of uncertainty extending to very low mixing ratios. However, all except one of the retrievals show no probability density for H_2O at solar or super-solar abundance for the Sheppard et al. (2017) data set. Such a sub-solar abundance, even with the inclusion of thermal dissociation, may have important consequences for the planetary atmosphere (see Section 4). The one exception is the case with H^- and without

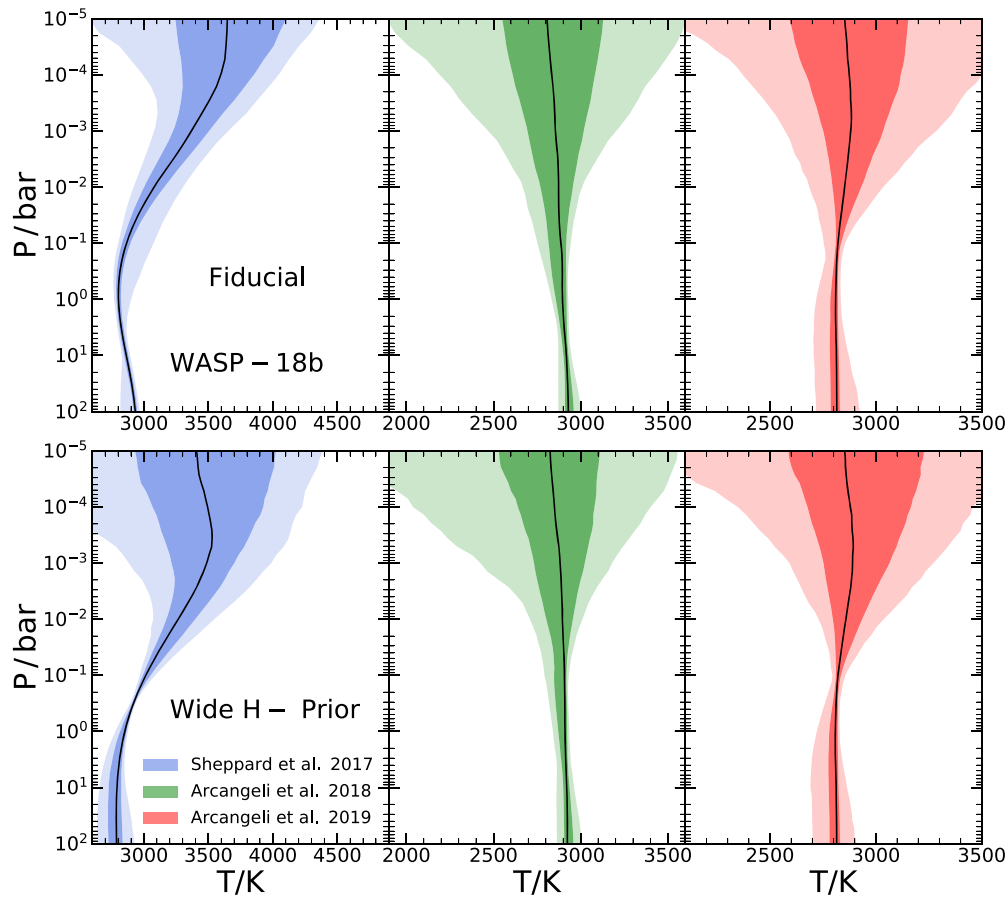


Figure 5. Retrieved pressure–temperature profiles for the retrievals conducted for WASP-18b. The left, middle, and right panels show the retrievals for the Sheppard et al. (2017), Arcangeli et al. (2018), and Arcangeli et al. (2019) data sets, respectively. The top panel for each data set shows the fiducial case, and the bottom panels show the case with a wide H- prior. The dark and light colors indicate the 1σ and 2σ uncertainty, respectively, with the solid black line showing the median best fit.

dissociation, which indicates no significant peak at any abundance and constrains the 2σ upper limit for H_2O to be $\log(\text{H}_2\text{O}) \sim -0.7$ (see Table 3).

Retrievals with Arcangeli et al. (2018) do not show any constraints on H_2O for any of the five cases run (see Table 3). The H_2O abundance retrieved from the H- and dissociation models is shown in Figure 3 and indicates no significant peak at any abundance. We constrain the 2σ upper limit to be $\log(\text{H}_2\text{O}) \sim -0.5$. This lack of constraint is likely due to the featureless WFC3 spectrum and Spitzer points, which lie along the ~ 2900 K isotherm (see Figure 2). This data set constrains a much more isothermal temperature profile as discussed below in Section 3.4. H_2O thus does not have features in the spectrum regardless of its abundance due to the lack of a significant temperature gradient. Hence, the inclusion of H- and dissociation into the model does not help constrain the abundance. In fact, as with the Sheppard et al. (2017) data set, the inclusion of H- and dissociation in these retrievals further increases the uncertainty on the H_2O as well as being statistically disfavored by the Bayesian analysis.

The Arcangeli et al. (2019) data set shows better constraints on the H_2O than the Arcangeli et al. (2018) data. All of the conducted retrievals showed a peak near the expected solar value but with a long tail in probability at both low and high abundance, meaning that, as with the other data sets, there is no definitive detection of H_2O . The HST WFC3 data does indicate a slightly lower planet/star flux ratio than the other two data sets, with a blackbody fit closer to 2800 K (Figure 2), but this is consistent with the fact that

the Arcangeli et al. (2019) data set samples cooler regions of the planetary disk, as stated in Section 1. We also see a median P–T profile with an inversion for this data set, but the constraints may also allow for an isothermal/non-inverted profile given the uncertainties (see Section 3.4). There are a handful of data points at $\sim 1.5 \mu\text{m}$, which indicate a potential emission feature from H_2O . This small rise in the spectrum near the H_2O feature is therefore able to constrain the H_2O to a greater degree than for the other two data sets.

3.2. H- Abundances

H- also has a nonnegligible cross section in the WFC3 bandpass, but we see no conclusive detection in any data set. Figure 3 shows the H- abundance for each of the three data sets for the fiducial and wide H- prior cases. Despite the strong cross section of H- in the WFC3 range and a spectral feature at $\sim 1.6 \mu\text{m}$, the H- abundance cannot be well constrained for almost any of the data sets due to the relatively featureless spectra. As thermal dissociation is included, the constraint on the H- abundance becomes weaker due to its lower abundance in the upper atmosphere.

Our fiducial model with the Sheppard et al. (2017) data shows two distinct modes in the posterior distribution. One mode consists of a super-solar H-, solar CO, and sub-solar H_2O distribution, while the other suggests a sub-solar H-, super-solar CO, and slightly sub-solar H_2O . This can be seen in the double-peaked posterior distribution of each species in the top

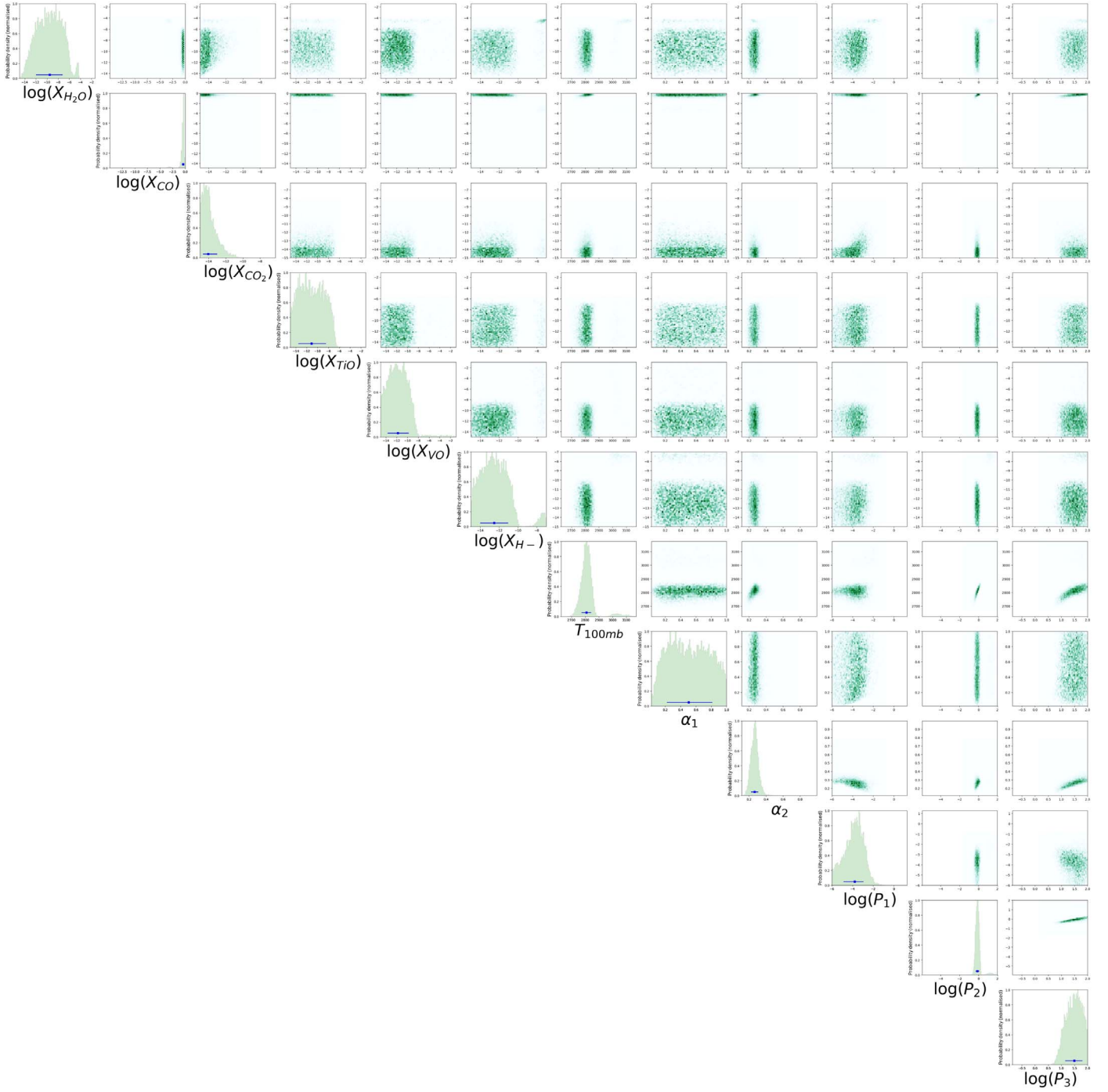


Figure 6. Posterior distribution for the fiducial retrieval of WASP-18b’s dayside spectrum from the Sheppard et al. (2017) data set. We retrieve six parameters representing the undissociated abundance of the chemical species and six parameters parameterizing the P–T profile as discussed in Madhusudhan & Seager (2009).

panels of Figure 3, particularly evident for H-. This arises due to the slight dip in the $1.6 \mu\text{m}$ data for the Sheppard et al. (2017) data set shown in Figure 2. This feature may be explained by the presence of CO or H-, given that both species have overlapping weak spectral features at this wavelength (see Figure 1). However, due to the weaker cross section of CO at $\sim 1.6 \mu\text{m}$, a very high abundance of $\log(\text{CO}) \sim -0.4$ is required for CO to explain the dip in the observations. We show the full posterior distribution for the fiducial retrieval of the Sheppard et al. (2017) data set in Figure 6.

When the H- abundance is unrestricted and allowed to extend up to $\log(\text{H-}) = 0$ for the case of the wide prior, the super-solar H- mode is preferred as shown in Figure 3 and the posterior distribution in Figure 7. This is because the H- possesses a strong bound-free opacity to explain the feature at the red end of the data. The predicted solar value from Parmentier et al. (2018) is $\log(\text{H-}) \approx -8.3$, while our undissociated H- abundance constraint is $\log(\text{H-}) = -3.4^{+2.1}_{-2.2}$ as shown in Table 3. Such an extremely high H- abundance is highly unphysical from chemical models (e.g., Parmentier et al. 2018). Therefore, the

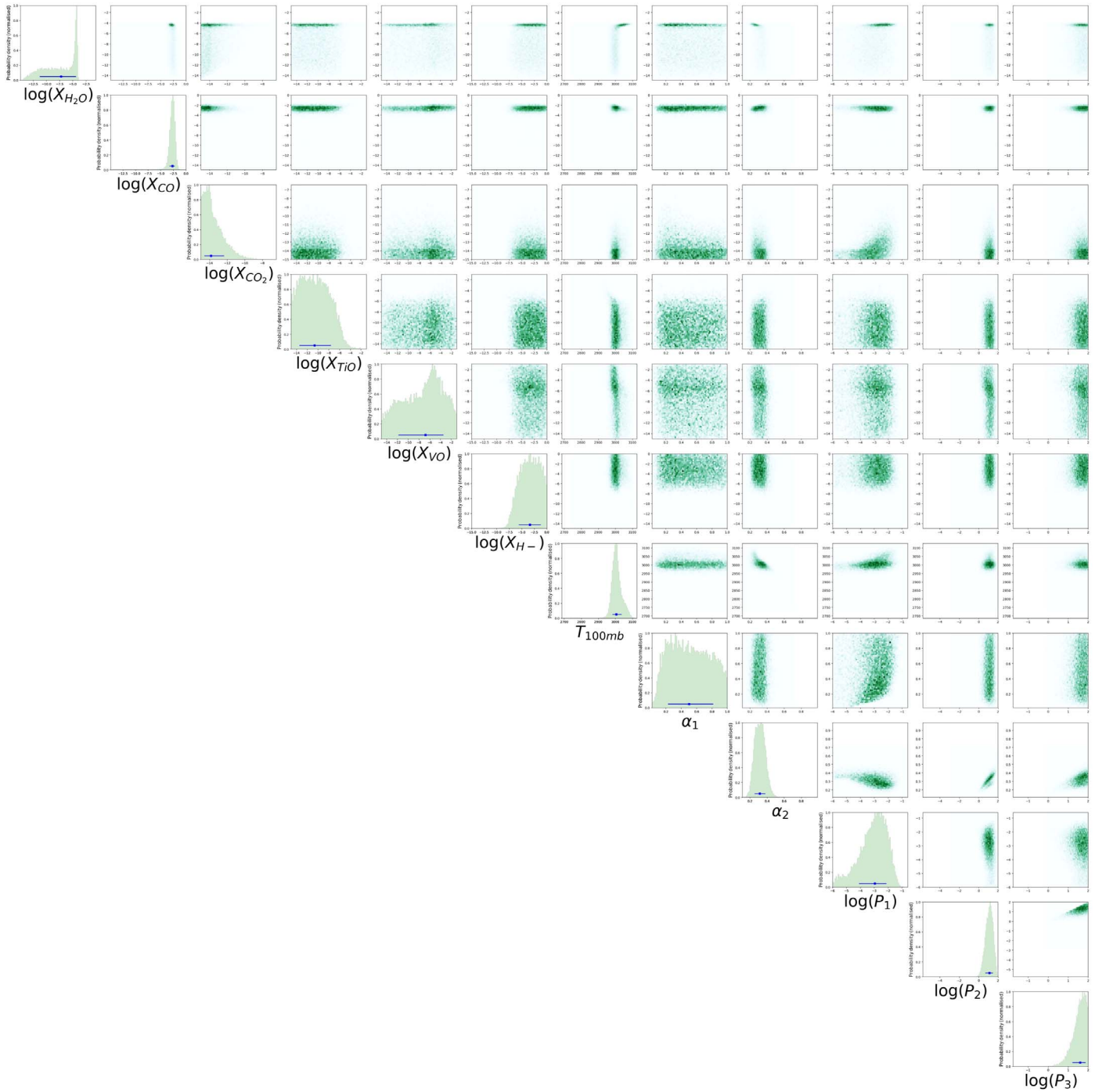


Figure 7. Posterior distribution for the wide H- prior retrieval of WASP-18b’s dayside spectrum from the Sheppard et al. (2017) data set. We retrieve six parameters representing the undissociated abundance of the chemical species and six parameters parameterizing the P–T profile as discussed in Madhusudhan & Seager (2009).

derived H- abundance in the wide prior case is an artifact of the degeneracy with CO given the dependence on a few data points near $1.6 \mu\text{m}$. We tested this conclusion by performing a retrieval without the final four data points at the red end of the WFC3 and found no constraint on the H- abundance. This super-solar H- mode in the wide prior retrieval is weakly disfavored over the fiducial case and strongly disfavored over a model without either H- or dissociation (see Table 3). This is because the extra H- parameter introduced into the retrievals does not change the evidence significantly to explain the observations better. In either case, the H_2O abundance remains sub-solar given that there is no

prominent spectral signature in the observations at $\sim 1.4 \mu\text{m}$ indicating its presence.

We further investigated the two modes in the posterior distribution for the Sheppard et al. (2017) data set by plotting the best-fitting models with varying H- abundances as shown in Figure 4. This shows that for the low H- mode, the spectrum is largely determined by the $\text{H}_2\text{-H}_2/\text{H}_2\text{-He}$ collisionally induced absorption and the CO absorption. The H_2 and CO are present in roughly equal parts at high abundance and, thus, are the only two species to significantly affect the spectrum. On the other hand, the spectrum for the high H- mode is determined by the

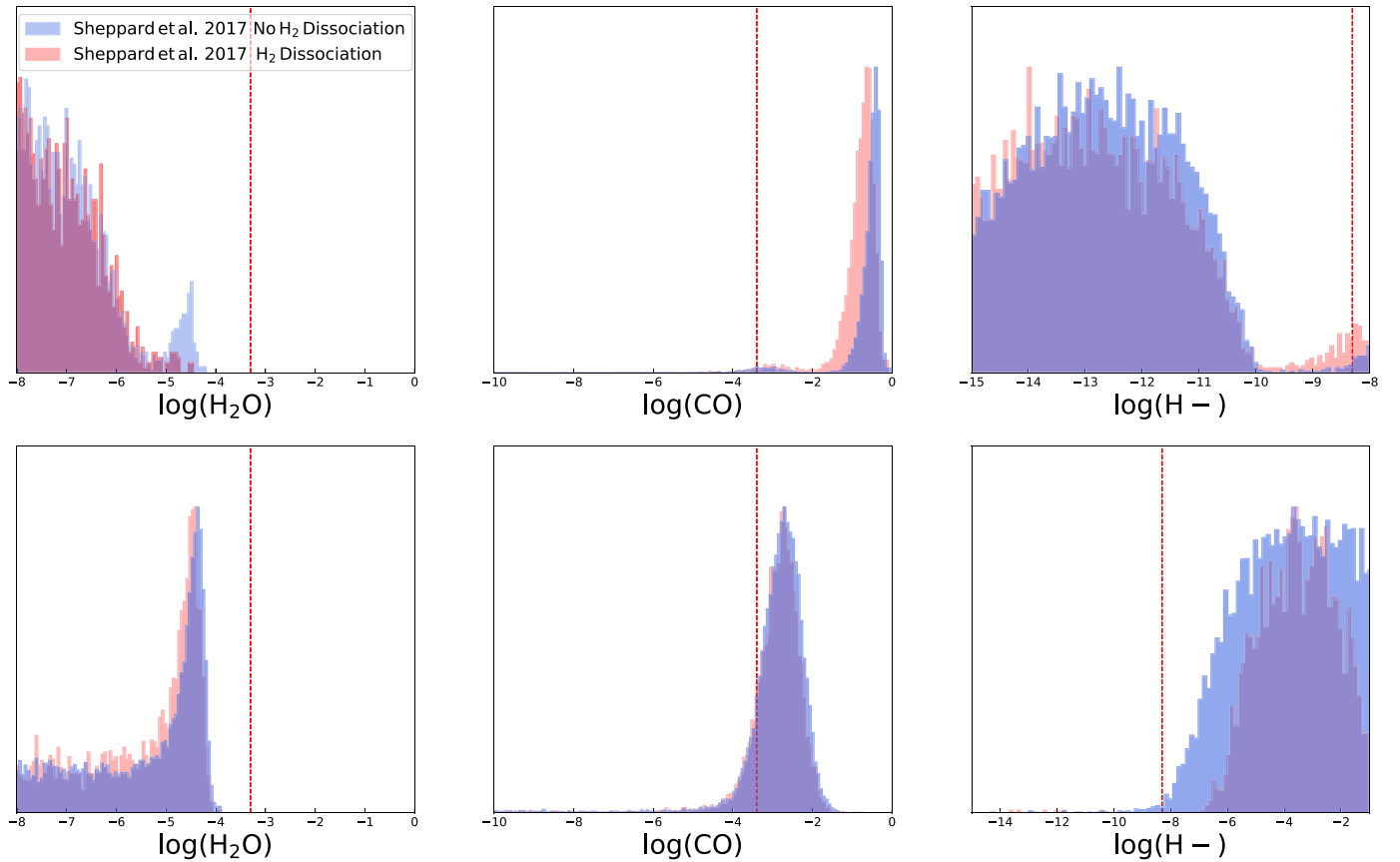


Figure 8. Posterior probability distributions of undissociated H_2O , CO, and H- abundances for the retrievals of the Sheppard et al. (2017) data set. The red and blue histograms show the retrievals with and without H_2 dissociation, respectively. The top panels show the fiducial case where the H- prior was restricted to be between $\log(\text{H}^-) = -15$ and -7 , whereas the bottom panel shows the wide prior case where the upper H- prior was extended to $\log(\text{H}^-) = 0$. The red dashed line shows the expected abundance for each of the species assuming chemical equilibrium with solar elemental abundances (Parmentier et al. 2018).

strong opacity of H- at such high abundances and also partly by the H_2O opacity due to the weak peak near $\sim 1.55 \mu\text{m}$. Intermediate H- abundances however are disfavored as they are unable to match the observations. We note that the narrow peak near $\sim 1.28 \mu\text{m}$ is a stellar feature.

We have also tested retrievals for the Sheppard et al. (2017) data set, which include the dissociation of H_2 , but we see no significant differences in the retrieved parameters as shown in Figure 8. This is because the deep atmosphere where the continuum is set is not strongly affected by the dissociation of H_2 , which occurs more significantly at high altitudes. Therefore, the CIA opacity is not significantly altered, and thus, the spectrum and the bimodal retrieved constraints are largely unchanged. The dissociation of H_2 was statistically favored in the fiducial retrieval but disfavored in the wide prior retrieval. Thus, we cannot conclusively confirm the dissociation of H_2 within the atmosphere based on current data.

The other two data sets do not show any constraint for H- for any of the retrievals conducted. These data sets have more isothermal P-T profiles without a potential spectral signature at $\sim 1.6 \mu\text{m}$, which makes constraints on H- very weak. We therefore see no strong evidence for H- in any of the data sets, at odds with previous work (Arcangeli et al. 2018), which indicated a detection of H- and a thermal inversion from equilibrium models. Our retrievals explored a wide range of temperatures and abundances and found that the featureless HST WFC3 spectrum cannot fully constrain H- definitively. A

weak preference for H- without thermal dissociation at a 1.1σ significance is seen in the Arcangeli et al. (2019) data set (see Table 3), but further observations of WASP-18b may be able to provide more stringent constraints on H-.

3.3. CO Abundances

The Spitzer photometric observations show an emission feature in the $4.5 \mu\text{m}$ band for the Sheppard et al. (2017) data set (see Figure 2). This is likely due to CO, which has a strong cross section at $\sim 4.5 \mu\text{m}$ (see Figure 1). The retrieved CO abundance is shown in Figure 3. The H- and H_2O opacities are weaker than that of CO at these wavelengths (see Figure 1), and thus, the $4.5 \mu\text{m}$ Spitzer point can only be well explained by the presence of CO. We find a median CO abundance of $\log(\text{CO}) = -0.41^{+0.15}_{-0.28}$ for our fiducial retrieval of the Sheppard et al. (2017) data set including H- and dissociation. The slightly stronger emission feature at $4.5 \mu\text{m}$ in the reanalyzed Sheppard et al. data set also constrains a stronger thermal inversion in the photosphere (see Figure 5). These results agree well with previous retrievals in Sheppard et al. (2017) with one exception. Our wide prior H- retrieval results in a lower CO abundance of $\log(\text{CO}) = -2.70^{+0.45}_{-0.57}$. This is because the H- abundance provides enough continuum opacity in the $4.5 \mu\text{m}$ band to allow for a lower CO abundance to explain the observed flux excess in that band.

The constraints on the CO abundances are weaker for the remaining two data sets due to the larger uncertainties in their 3.6 and 4.5 μm Spitzer data obtained from Maxted et al. (2013). Our fiducial case constrains CO at $\log(\text{CO}) = -4.0^{+3.6}_{-5.6}$ and $\log(\text{CO}) \lesssim -0.3$ for the Arcangeli et al. (2018) and Arcangeli et al. (2019) data sets, respectively. The retrievals on the Arcangeli et al. (2018) data set do still indicate a modal CO value at super-solar abundance ($\log(\text{CO}) \sim -1$) (see Figure 3), but the uncertainty is much greater, and the distributions have long tails extending to significantly lower abundances. Therefore, the median abundances and uncertainties retrieved allow for solar as well as super-solar CO abundances, as shown in Table 3. The retrieved CO abundances are largely unaffected by the inclusion of thermal dissociation and H- opacity. This is unsurprising given that CO does not thermally dissociate at such temperatures, and any H- present would only contribute relatively weaker free-free absorption in the Spitzer bandpass at physically plausible quantities (see Figure 1). The Arcangeli et al. (2019) data set does not show any significant constraints on the CO, as the Spitzer observations from Maxted et al. (2013) largely follow a blackbody spectrum (see Figure 2).

We tested whether the Spitzer data was indeed the source of the CO abundance and thermal inversion constraints by retrieving each data set with only the HST WFC3 observations. All except one showed a temperature profile that was isothermal, given that the WFC3 spectrum is largely featureless, and there is no constraint on any species. The Sheppard et al. (2017) data set was the outlier and showed a bimodal CO constraint due to the slight downturn in the WFC3 points near 1.6 μm , similar to that seen in the fiducial case discussed previously in Section 3.2. The CO has molecular absorption in the WFC3 range near the H- feature at $\sim 1.6 \mu\text{m}$ (see Figure 4), and therefore, it is not unexpected that the dip in the WFC3 points may be explained by either species. Our retrievals show evidence for either CO or H-, the former of which was claimed in Sheppard et al. (2017) given that H- was not included in their analysis. This constraint on CO is however much weaker than with the inclusion of the Spitzer photometric bands, where CO has a much stronger feature near $\sim 4.5 \mu\text{m}$ (see Figure 1). The arrival of the James Webb Space Telescope (JWST) is therefore likely to place much stronger constraints on the CO abundance due to its higher precision and higher-resolution observations covering this CO absorption feature.

3.4. P–T Profile

Figure 5 shows the P–T profiles for the fiducial and the wide H- prior retrievals for each data set. Our work shows that the best constraints on the P–T profile occur in the photosphere probed at $P \sim 0.1$ bar, where most of the emission occurs. Lower pressures ($P \lesssim 10^{-3}$ bar) show a much less constrained temperature given that they have a negligible effect on the spectrum. The effect is similar at higher pressures ($P \gtrsim 10$ bar) where the onset of the isotherm and the high optical depth limit our ability to constrain the P–T profile. However, there are some key differences in the retrieved P–T profiles, which we explore below.

The Sheppard et al. (2017) retrievals show a thermal inversion present in the photosphere ($P \sim 100$ mbar) with a $T_{100 \text{ mb}} \sim 2800$ – 3000 K. This inversion is primarily constrained by the Spitzer photometric data, which show a strong CO emission feature at 4.5 μm . We see an inversion present in every retrieval run for this data set, with and without H- or

dissociation. This data set shows the strongest thermal inversion of all three data sets with a temperature increase of ~ 600 K going upwards in the atmosphere as shown in Figure 5. However, our results in Arcangeli et al. (2018) indicate a more isothermal P–T profile. This is caused by the weaker Spitzer constraints from the Maxted et al. (2013) observations with larger error bars as well as the featureless WFC3 data. These points all mostly lie along the isotherm of ~ 2900 K, and hence, we do not see much variation whether H- or dissociation is included. Equilibrium models from Arcangeli et al. (2018) indicated the presence of a thermal inversion in the upper atmosphere, and our results do allow for a thermal inversion at pressures $\lesssim 10^{-2}$ bar given that the temperature is less well constrained in the upper atmosphere. Hence, despite the largely isothermal profile, the large uncertainty does mean that we constrain the P–T profile to be within 2σ of that reported in Arcangeli et al. (2018).

The spectra of Arcangeli et al. (2019) showed an inversion similar to but weaker than that of Sheppard et al. (2017) due to the less well-constrained emission features from CO in the Spitzer 4.5 μm band. The slightly lower planet/star flux ratio in the WFC3 and Spitzer bands also constrains a slightly cooler temperature at $T_{100 \text{ mb}} \sim 2800$ K as shown in Table 3, which may be ascribed to the different phase sampling for this data set as discussed in Section 1. Generally, we see a 100 mbar temperature that is very close to the expected dayside photospheric temperature of WASP-18b without significant redistribution for all three of the data sets.

We additionally tested whether our assumed stellar temperature (given in Table 1) affected the results by varying the stellar temperature by 100 K (the 1σ error in its value) and rerunning our retrievals. We found no significant change to the retrieved results for any of the parameters. We did see a change in the peak in the distribution for the 100 mbar temperature by ~ 45 K, as expected in order to match the observed planet/star flux ratio in the data set.

3.5. Constraints on Other Species

Our retrievals are unable to constrain TiO or VO significantly. Thermal inversions have been predicted from equilibrium models of hot Jupiters due to species such as TiO and VO (Fortney et al. 2008; Spiegel et al. 2009). In our retrievals, we only observe very weak constraints for TiO using the Arcangeli et al. (2018) data set, which shows a peak at $\log(\text{TiO}) \sim -6$ (see Figure 9) but with a long-tailed distribution at low and high abundance. The Arcangeli et al. (2019) data set also showed a broad peak at unphysically high abundances of $\log(\text{TiO}) \sim -3$, as shown in the posterior distribution in Figure 10. This also has a large uncertainty and tail to lower values. Expectations from solar abundances (Asplund et al. 2009) and equilibrium models of WASP-18b (Lothringer et al. 2018; Parmentier et al. 2018) indicate that these species should be present at $\log(\text{TiO}) \sim -7$ and $\log(\text{VO}) \sim -9$ (Asplund et al. 2009). The atmosphere of WASP-18b may also be more susceptible to thermal inversions from species such as TiO and VO if the H₂O abundance is sub-solar, as indicated by the Sheppard et al. (2017) data or thermally dissociated. This is because the presence of strong infrared opacity (such as H₂O) can act to cool the upper atmosphere due to its radiative efficiency, thereby reducing the heating effectiveness of species such as TiO and VO (Mollière et al. 2015; Gandhi & Madhusudhan 2019). Therefore, a low H₂O abundance makes thermal inversions more likely.

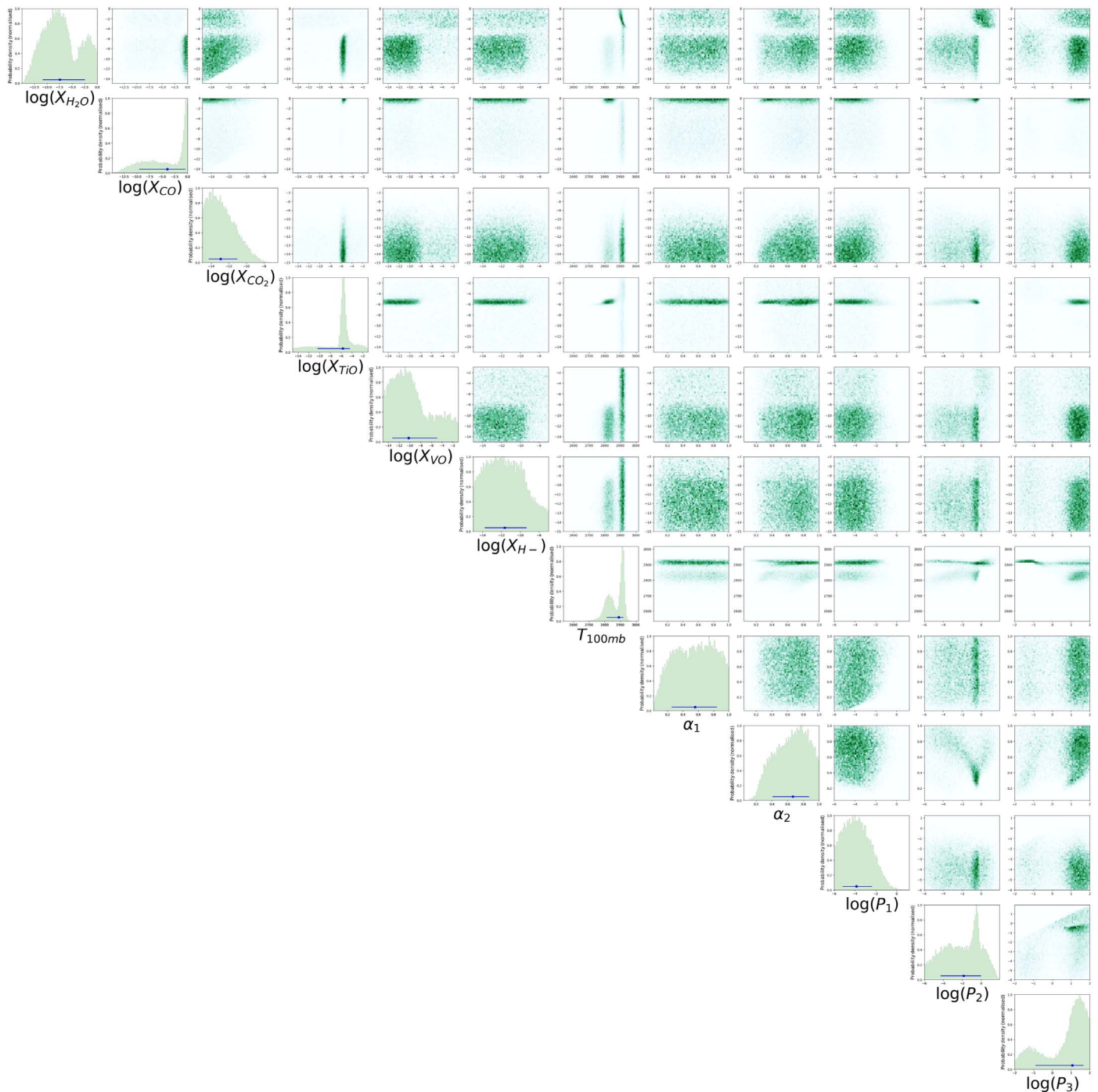


Figure 9. Posterior distribution for the fiducial retrieval of WASP-18b’s dayside spectrum from the Arcangeli et al. (2018) data set. We retrieve six parameters representing the undissociated abundance of the chemical species and six parameters parameterizing the P–T profile as discussed in Madhusudhan & Seager (2009).

We also do not constrain the CO_2 abundance significantly. Previous theoretical studies have also shown that CO_2 is rarely dominant over H_2O and CO in hot Jupiter atmospheres (Madhusudhan 2012; Moses et al. 2013; Heng & Lyons 2016). We thus limit our model to include $\log(\text{CO}_2) \leq \log(\text{CO})$ and $\log(\text{CO}_2) \leq \log(\text{H}_2\text{O})$. This also allows us to break the degeneracy between CO and CO_2 in the $4.5 \mu\text{m}$ Spitzer band, where both of these species have strong absorption (Madhusudhan & Seager 2010; Kreidberg et al. 2014; Gandhi & Madhusudhan 2018).

4. Summary and Discussion

We present here a case study of retrieval analysis for UHJ atmospheres with equilibrium temperatures in excess of 2000 K. We focus on the UHJ WASP-18b. The motivation for this work arises from recent work on equilibrium models of such ultra-hot planets, which show that H- opacity and thermal dissociation of species such as H_2O may be important (Arcangeli et al. 2018; Kreidberg et al. 2018; Lothringer et al. 2018; Parmentier et al. 2018; Mansfield et al. 2018). To

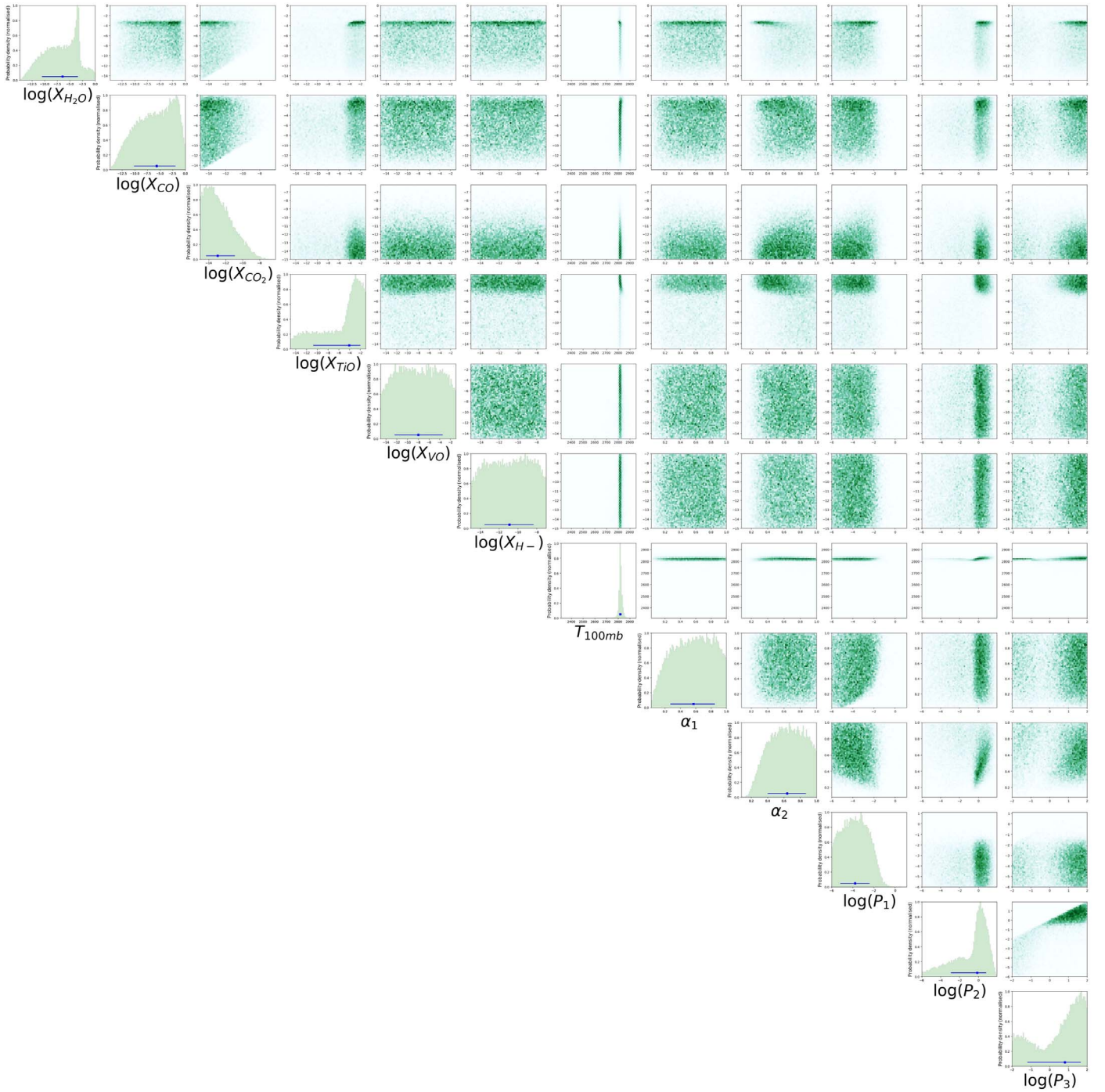


Figure 10. Posterior distribution for the fiducial retrieval of WASP-18b’s dayside spectrum from the Arcangeli et al. (2019) data set. We retrieve six parameters representing the undissociated abundance of the chemical species and six parameters parameterizing the P–T profile as discussed in Madhusudhan & Seager (2009).

achieve this, we have extended our recently developed HyDRA model (Gandhi & Madhusudhan 2018) in order to retrieve the dissociated abundances of numerous species as well as the H-mixing ratio within the atmosphere. To study the effect of H- and dissociation, we carry out five separate retrievals on each of the three available data sets with dayside observations of the hot Jupiter WASP-18b (Sheppard et al. 2017; Arcangeli et al. 2018, 2019).

We do not find strong evidence for H- in any of the data sets. The retrievals of the Arcangeli et al. (2018) and Arcangeli et al. (2019) data sets show no significant constraints on any species

when H- and dissociation are included (see Figure 3). On the other hand, the Sheppard et al. (2017) data set does show two distinct families of solutions depending on the H- prior. With a wide H- prior, the data favor a super-solar H- abundance of $\log(\text{H}^-) = -3.4^{+2.1}_{-2.2}$, which is $\sim 4\text{--}6$ orders of magnitude greater than that predicted from the dayside equilibrium models of WASP-18b (Arcangeli et al. 2018). However, our fiducial case with an H- prior restricted to more realistic values ($\log(\text{H}^-) \lesssim -7$) constrains only an upper limit on the H- that is consistent with solar abundance. However, the fiducial retrieval constrains a super-solar CO abundance of

$\log(\text{CO}) = -0.41_{-0.28}^{+0.15}$. This value is between ~ 2 – 4 orders of magnitude greater than solar abundance (Madhusudhan 2012; Moses et al. 2013), which also may not be realistic.

We are therefore currently left with two possibly unphysical families of solutions, and we must wait for improved data in the future to narrow our solution space. However, for almost all retrievals for the currently available data sets, the inclusion of H- and thermal dissociation is statistically disfavored as shown in Table 3. We thus do not see any strong evidence for H- in any of the dayside observations for WASP-18b, counter to that reported in Arcangeli et al. (2018). However, we do suggest that H- be included as a retrieval parameter for analyses of UHJs ($T_{\text{eq}} \gtrsim 2000$ K) despite the fact that we are unable to detect it given that it does have the potential to influence the spectrum in the HST WFC3 range (e.g., Arcangeli et al. 2018; Lothringer et al. 2018; Parmentier et al. 2018; Mikal-Evans et al. 2019).

Without any significant spectral features in the WFC3 observations, we find that H_2O is also undetected in our current work. We retrieved the H_2O abundances for each of the data sets, with and without H- or dissociation. We saw good agreement between these, as shown in Table 3. We constrain an upper limit for H_2O that is slightly sub-solar for the Sheppard et al. (2017) data set, even with the inclusion of dissociation and H- opacity. The Arcangeli et al. (2019) data set similarly indicates a weak peak for H_2O but closer to solar composition. The Arcangeli et al. (2018) data on the other hand do not show significant H_2O constraints given the more isothermal temperature profile that is retrieved (see Figure 5). We therefore conclude that the inclusion of H- and/or thermal dissociation in our retrievals does not help to fully constrain the H_2O abundance. Further observations, either with improved wavelength coverage and sensitivity or perhaps through transmission spectroscopy, may be required to resolve this conundrum.

We find different constraints on the CO abundance depending on the data sets. Retrievals with the Sheppard et al. (2017) data set were the only ones that showed a clear detection peak for CO due to the smaller error bars on the Spitzer data. The expected CO abundance from chemical equilibrium models is $\log(\text{CO}) \approx -3.4$ (Madhusudhan 2012; Moses et al. 2013), and our retrievals constrained CO to be between $\log(\text{CO}) = -2.70_{-0.57}^{+0.45}$ and $\log(\text{CO}) = -0.41_{-0.28}^{+0.15}$ depending on the H- prior (see Table 3). This is due to its degeneracy with H- as discussed in Section 3.2. A super-solar CO abundance was reported in Sheppard et al. (2017) from retrievals without H-, and Arcangeli et al. (2018) used equilibrium models to argue the importance of H- opacity and obtained a solar CO abundance. Our retrievals indicate that both proposed explanations are able to fit the observations for the Sheppard et al. (2017) data, but one of either CO or H- has to be super-solar. Neither of the other two data sets showed any significant constraints on CO, with only a weak super-solar peak seen in the retrievals of the Arcangeli et al. (2018) data set.

Determining the CO abundance is crucial, as this has been shown to be a good proxy for the metallicity (Madhusudhan 2012). It does not vary significantly with the atmospheric C/O ratio for temperatures in excess of ~ 1500 K and does not thermally dissociate at the temperatures typical for UHJs (e.g., Moses et al. 2013; Parmentier et al. 2018). For a solar composition atmosphere, the CO abundance is $\log(\text{CO}) \approx -3.4$ (Madhusudhan 2012; Moses et al. 2013). The super-solar CO abundances seen for some of the retrievals for the Sheppard et al. (2017) data set may thus indicate a very high metallicity, while others are consistent with near-solar abundance. Additionally, the retrievals with the

Arcangeli et al. (2018) and Arcangeli et al. (2019) data sets are also consistent with solar metallicity given their larger uncertainties. Hence, future work that can improve the CO abundance constraints may be able to better constrain the metallicity of WASP-18b.

The stronger $4.5 \mu\text{m}$ emission feature in the Spitzer observations also constrained a thermal inversion in the Sheppard et al. (2017) data set as shown in Figure 5. That of Arcangeli et al. (2018) on the other hand constrained a much more isothermal temperature profile given that the Spitzer data had larger error bars, and the HST WFC3 spectra are all largely featureless and lie along the same isotherm ($T \sim 2900$ K). The Arcangeli et al. (2019) data set showed evidence for a thermal inversion but with weaker constraints than the Sheppard et al. (2017) data set.

We note that our retrievals do differ from the equilibrium models used in Arcangeli et al. (2018) for their inference of H-. Our work assumes that the abundances of the chemical species can be treated as free parameters, whereas the equilibrium models used in Arcangeli et al. (2018) assume that the abundances are in chemical equilibrium and can be derived from the stellar redistribution, metallicity, and C/O ratio. Hence, our retrievals allow for chemical species not in thermochemical equilibrium. In addition, Arcangeli et al. (2018) use radiative-convective equilibrium P–T profiles, which indicate the presence of thermal inversions in the upper atmosphere. We parameterize the P–T profile, which allows us to explore a wide range of inverted, non-inverted, and isothermal profiles. Our retrievals indicate more isothermal or weakly inverted temperature profiles due to largely featureless data (see Figure 5). A precise balance of the overall infrared to visible opacity is required to achieve isotherms in an atmosphere (Guillot 2010; Mollière et al. 2015; Gandhi & Madhusudhan 2019), which may be unlikely for UHJs (e.g., Lothringer et al. 2018). In reality, we would expect both approaches of retrievals and grids of equilibrium models to converge to the same results in the presence of well-constraining data with strong spectral features, as was achieved on observations of WASP-43b (Gandhi & Madhusudhan 2018).

We should also highlight the assumptions within the dissociation model used in the retrievals. First, we have assumed that the ionization of H- may be parameterized in a similar way to the other species. In reality, the H- abundance is set by complex chemical interactions and is strongly dependent on the free electron abundance (Parmentier et al. 2018). Hence, this assumption breaks down away from solar composition. We use this parametric model for H- so we can perform a free chemical retrieval due to lack of a better prescription in such a case. A potential solution is to perform retrievals in chemical equilibrium and vary the C, O, and N abundance as was recently done for WASP-121b (Mikal-Evans et al. 2019).

We also leave the abundance of each species as a free parameter in our retrieval and assume that only this abundance and the temperature profile affect the thermal dissociation of each species. The dissociation reactions only involve the corresponding species and their dissociated byproducts (Parmentier et al. 2018), and they are unaffected by the abundances of other species. Thus, we can justify assuming the dissociating species are in chemical equilibrium with respect to thermal dissociation, even though we do not assume them to be in chemical equilibrium with respect to other species in the atmosphere.

This work represents a crucial step in the characterization of UHJs, which have recently come to the forefront thanks to high-precision observations (e.g., Haynes et al. 2015; Evans et al. 2017; Sheppard et al. 2017; Kreidberg et al. 2018). With such extreme

temperatures, our understanding of atmospheric processes has been pushed to the limit. For instance, theoretical models of planets with extreme irradiation with equilibrium temperatures well in excess of 2000 K are now being explored (e.g., Kitzmann et al. 2018; Parmentier et al. 2018). The high-temperature HyDRA retrieval framework may form the basis for compositional studies of UHJs as more observational data becomes available. WASP-18b is a JWST early release science target (Bean et al. 2018), and thus, we may soon be able to shed more light on these physical processes for UHJs and finally confirm the presence of H- and/or dissociation in the dayside atmosphere.

S.G. acknowledges support from the UK Science and Technology Facilities Council (STFC). We thank the anonymous referee for a careful review of our manuscript.

ORCID iDs

Siddharth Gandhi  <https://orcid.org/0000-0001-9552-3709>

Nikku Madhusudhan  <https://orcid.org/0000-0002-4869-000X>

Avi Mandell  <https://orcid.org/0000-0002-8119-3355>

References

- Arcangeli, J., Désert, J.-M., Line, M. R., et al. 2018, *ApJL*, 855, L30
- Arcangeli, J., Désert, J.-M., Parmentier, V., et al. 2019, *A&A*, 625, A136
- Asplund, M., Grevesse, N., Sauval, A. J., & Scott, P. 2009, *ARA&A*, 47, 481
- Bean, J. L., Stevenson, K. B., Batalha, N. M., et al. 2018, *PASP*, 130, 114402
- Beatty, T. G., Madhusudhan, N., Pogge, R., et al. 2017a, *AJ*, 154, 242
- Beatty, T. G., Madhusudhan, N., Tsiraras, A., et al. 2017b, *AJ*, 154, 158
- Bell, K. L., & Berrington, K. A. 1987, *JPhB*, 20, 801
- Buchner, J., Georgakakis, A., Nandra, K., et al. 2014, *A&A*, 564, A125
- Castelli, F., & Kurucz, R. L. 2003, in IAU Symp. 210, Modelling of Stellar Atmospheres, ed. N. Piskunov, W. W. Weiss, & D. F. Gray (San Francisco, CA: ASP), A20
- Deming, D., Wilkins, A., McCullough, P., et al. 2013, *ApJ*, 774, 95
- Drummond, B., Carter, A. L., Hébrard, E., et al. 2019, *MNRAS*, 486, 1123
- Evans, T. M., Sing, D. K., Kataria, T., et al. 2017, *Natur*, 548, 58
- Feroz, F., & Hobson, M. P. 2008, *MNRAS*, 384, 449
- Feroz, F., Hobson, M. P., & Bridges, M. 2009, *MNRAS*, 398, 1601
- Fortney, J. J., Marley, M. S., Saumon, D., & Lodders, K. 2008, *ApJ*, 683, 1104
- Gandhi, S., & Madhusudhan, N. 2017, *MNRAS*, 472, 2334
- Gandhi, S., & Madhusudhan, N. 2018, *MNRAS*, 474, 271
- Gandhi, S., & Madhusudhan, N. 2019, *MNRAS*, 485, 5817
- Guillot, T. 2010, *A&A*, 520, A27
- Haynes, K., Mandell, A. M., Madhusudhan, N., Deming, D., & Knutson, H. 2015, *ApJ*, 806, 146
- Heng, K., & Lyons, J. R. 2016, *ApJ*, 817, 149
- John, T. L. 1988, *A&A*, 193, 189
- Kitzmann, D., Heng, K., Rimmer, P. B., et al. 2018, *ApJ*, 863, 183
- Kreidberg, L., Bean, J. L., Désert, J.-M., et al. 2014, *ApJL*, 793, L27
- Kreidberg, L., Line, M. R., Parmentier, V., et al. 2018, *AJ*, 156, 17
- Kurucz, R. L. 1979, *ApJS*, 40, 1
- Lodders, K., & Fegley, B. 2002, *Icar*, 155, 393
- Lothringer, J. D., Barman, T., & Koskinen, T. 2018, *ApJ*, 866, 27
- Madhusudhan, N. 2012, *ApJ*, 758, 36
- Madhusudhan, N. 2019, *ARA&A*, 57, 617
- Madhusudhan, N., Crouzet, N., McCullough, P. R., Deming, D., & Hedges, C. 2014, *ApJL*, 791, L9
- Madhusudhan, N., Mousis, O., Johnson, T. V., & Lunine, J. I. 2011, *ApJ*, 743, 191
- Madhusudhan, N., & Seager, S. 2009, *ApJ*, 707, 24
- Madhusudhan, N., & Seager, S. 2010, *ApJ*, 725, 261
- Mansfield, M., Bean, J. L., Line, M. R., et al. 2018, *AJ*, 156, 10
- Maxted, P. F. L., Anderson, D. R., Doyle, A. P., et al. 2013, *MNRAS*, 428, 2645
- McKemmish, L. K., Masseron, T., Hoeijmakers, H. J., et al. 2019, *MNRAS*, 488, 2836
- McKemmish, L. K., Yurchenko, S. N., & Tennyson, J. 2016, *MNRAS*, 463, 771
- Mikal-Evans, T., Sing, D. K., Goyal, J. M., et al. 2019, *MNRAS*, 488, 2222
- Mollière, P., van Boekel, R., Dullemond, C., Henning, T., & Mordasini, C. 2015, *ApJ*, 813, 47
- Moses, J. I., Madhusudhan, N., Visscher, C., & Freedman, R. S. 2013, *ApJ*, 763, 25
- Nymeyer, S., Harrington, J., Hardy, R. A., et al. 2011, *ApJ*, 742, 35
- Parmentier, V., Line, M. R., Bean, J. L., et al. 2018, *A&A*, 617, A110
- Pinhas, A., Madhusudhan, N., Gandhi, S., & MacDonald, R. 2019, *MNRAS*, 482, 1485
- Richard, C., Gordon, I. E., Rothman, L. S., et al. 2012, *JQSRT*, 113, 1276
- Rothman, L. S., Gordon, I. E., Barber, R. J., et al. 2010, *JQSRT*, 111, 2139
- Sheppard, K. B., Mandell, A. M., Tamburo, P., et al. 2017, *ApJL*, 850, L32
- Shporer, A., Wong, I., Huang, C. X., et al. 2019, *AJ*, 157, 178
- Spiegel, D. S., Silverio, K., & Burrows, A. 2009, *ApJ*, 699, 1487
- Tennyson, J., Yurchenko, S. N., Al-Refaie, A. F., et al. 2016, *JMoSp*, 327, 73
- Wishart, A. W. 1979, *MNRAS*, 187, 59P